2026 IEEE International Conference on Robotics and Automation (ICRA 2026)
June 1-5, 2026. Vienna, Austria

Systematic Characterization of Drilling Parameters in Concentric Tube Steerable Drilling Robots: A comparative Study

Daniyal Maroufi*[1], Yash Kulkarni*[1], Vibhu Kana Rajesh Kana[2], Jordan P. Amadio[3], Mohsen Khadem[4], Justin E. Bird [5], Jeffrey H. Siewerdsen[6], and Farshid Alambeigi[1]

***Abstract*— To establish a foundational understanding for creating J-shaped trajectories with Concentric Tube Steerable Drilling Robots (CT-SDRs), this paper presents a systematic characterization of two operational factors: drill feed rate and rotational speed. We developed and compared a custom High-Speed Drill (HSD) and a Low-Speed Drill (LSD) to analyze how these parameters affect performance in flexible robotic drills versus conventional systems utilizing rigid instruments. By integrating the CT-SDRs with a seven degree-of-freedom robotic manipulator, we conducted experiments in synthetic bone phantoms of varying densities, assessing metrics such as motor current, hole diameter, radius of curvature, and drilling time. The results reveal critical performance trade-offs, demonstrating that high-speed drilling in CT-SDRs is essential for successfully penetrating dense bone. Further, we found that while slower feed rates improve trajectory accuracy and reduce hole enlargement, they significantly increase procedural time. These findings offer a quantitative guideline for design choices, component selection, and operational control of CT-SDRs tailored to patient-specific bone quality.**

I. Introduction

Spinal Fixation (SF) is a common and critical procedure for treatment of a wide range of spinal disorders ranging from spinal tumors to vertebral compression fractures, with Pedicle Screw Fixation (PSF) being the gold standard for treatment [1], [2]. Despite it's widespread application, the efficacy of PSF is challenged by the complex anatomy of the vertebral bodies. This complex anatomy of the vertebrae limits a surgeon's maneuverability and makes it difficult to achieve optimal drilling and screw placement angles, particularly in patients with low bone mineral density (BMD) where the risk of fixation failure and screw pullout is elevated [3], [4]. The difficulty of navigating instruments around vital structures can further lead to significant complications, such as nerve root, vascular, and spinal cord injuries [5]. To partially address these challenges, surgical navigation systems and commercially available robotic platforms such as ExcelsiusGPS and Mazor X were developed [6]. By creating 3D models of the patient's anatomy and tracking instruments in real-time, these technologies have successfully reduced the risk of screw misplacement and possible injuries [6], [7].

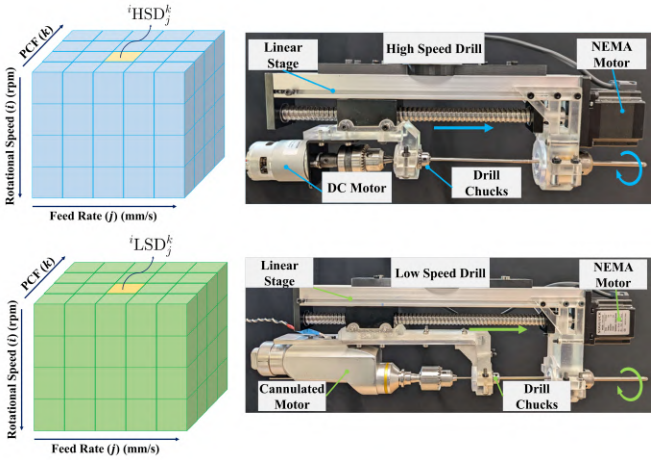

Fig. 1. (Top) 3D tensor representation of the experimental parameter space defined by feed rate, rotational speed, and Sawbones density, alongside the high-speed drill with labeled components. (Bottom) Corresponding 3D tensor and low-speed drill setup with labeled components.

While these robotic platforms are competent at guiding tools along a predefined straight-line path, their functionality is fundamentally limited by this reliance on rigid instrumentation. They act as precise guides but cannot alter the linear nature of the trajectory itself. This presents a significant clinical uncertainty, especially in osteoporotic patients, where the regions of highest BMD needed for robust screw purchase may not lie along a straight path from a safe entry point on the pedicle [8], [9]. Consequently, surgeons are often forced to compromise between a biomechanically superior but potentially risky trajectory and a safer trajectory that may result in suboptimal fixation, leaving the patient vulnerable to implant loosening or failure.

To overcome this critical gap, Steerable Drilling Robots (SDRs) have emerged as a major advancement in spinal robotics [10], moving beyond simple guidance to enable curved trajectories within vertebral bone [11]–[13]. Sharma et. al. [14]–[16] contributed to this area by developing

*These authors contributed equally to this work.

**This work was supported by the Collaborative Accelerator for Transformative Research Endeavors grant, jointly awarded by The University of Texas at Austin and The University of Texas MD Anderson Cancer Center.

[1]D. Maroufi, Y. Kulkarni and F. Alambeigi are with the Walker Department of Mechanical Engineering and Texas Robotics at The University of Texas at Austin, Austin, TX, 78712, USA. Email: {maroufi, kulkarni.yash08}@utexas.edu, farshid.alambeigi@austin.utexas.edu

[2]V. Rajesh Kana is with the Department of Biomedical Engineering and Texas Robotics at The University of Texas at Austin, Austin, TX, 78712, USA.

[2]J. P. Amadio is with the Department of Neurosurgery, The University of Texas Dell Medical School, TX, 78712.

[4]M. Khadem is with the School of Informatics, University of Edinburgh, UK.

[5]J. E. Bird is with the Department of Orthopedic Oncology, Division of Surgery, The University of Texas M.D. Anderson Cancer Center, Houston, TX, USA.

[6]J. H. Siewerdsen is with the Department of Imaging Physics, Division of Diagnostic Imaging, The University of Texas MD Anderson Cancer Center, Houston, Texas, USA.

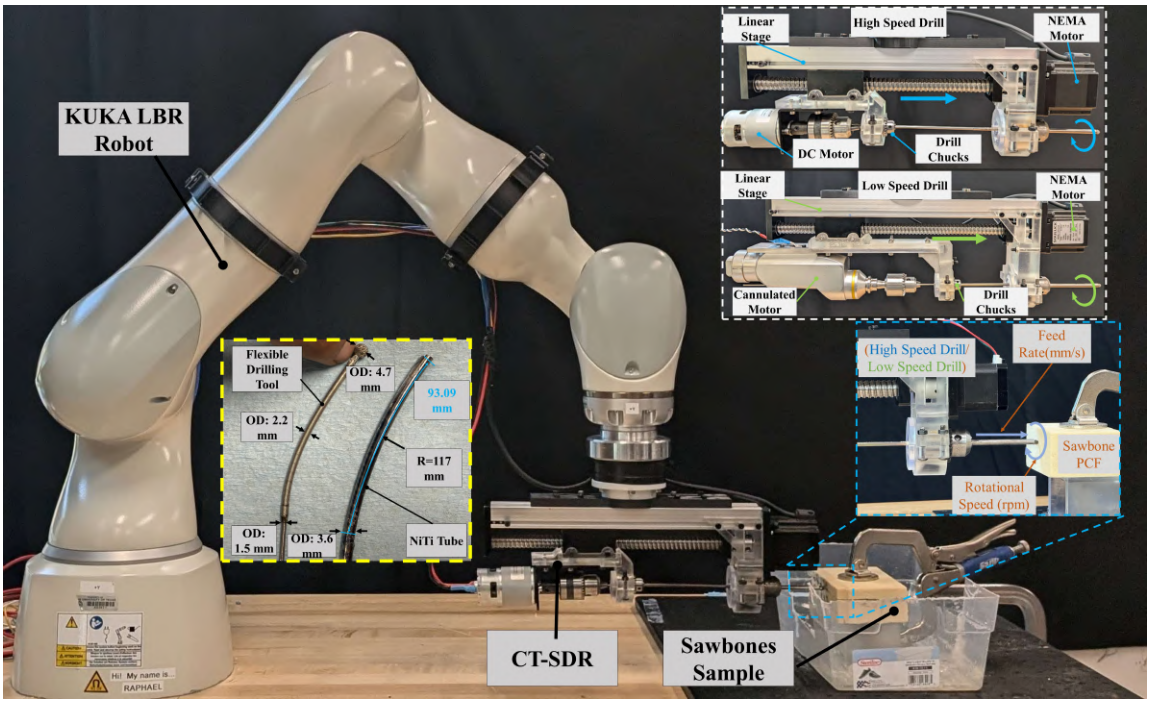

Fig. 2. Experimental setup with a KUKA LBR 14 robot with CT-SDR system. The setup includes the flexible drilling tool and NiTi tube samples with outer diameters and radius of curvature labeled, and Sawbone specimens. The two drill assemblies, parameter space (feed rate, rotational speed, Sawbone PCF), and labeled components of the drilling platforms are highlighted.

the Concentric Tube Steerable Drilling Robot (CT-SDR), a system designed specifically to address the limitations of linear approaches. The key benefit of the CT-SDR is its ability to create non-linear, curved paths (such as C-, J-, and S-shaped trajectories) after entering the pedicle [17]. This capability allows the drill to navigate around anatomical constraints and intentionally target regions of high BMD within the vertebral body that are otherwise inaccessible to rigid tools. By enabling fixation in these denser bone regions, the CT-SDR provides a method to significantly enhance the pullout strength of the pedicle screw, directly improving the long-term stability of the spinal implant [18]–[20]. Maroufi et al. [21] advanced this technology by introducing a framework for more realistic robotic spinal fixation procedures. This framework employed a four-phase approach to drilling through regions of differing bone density, simulating the harder cortical and softer cancellous bone. By integrating an enhanced CT-SDR with a 7-degree-of-freedom manipulator and the proposed framework, they achieved autonomous, patient-specific drilling patterns in a more clinically realistic setup. Their work was also pivotal in advancing towards clinically relevant pilot hole sizes by combining rigid and flexible drilling tools, marking an important step for pedicle screw fixation (PSF).

While significant progress has been made in development of this steerable drilling technology for creating complex curvilinear trajectories, the aforementioned studies (e.g. , [14], [22], [23] and [21]) mostly were focused on design of the drilling device and development of the robotic platform and not quantitative evaluation of the operational parameters. These studies relied on fixed and potentially suboptimal operational parameters, such as drill feed rate (i.e. insertion speed of the drill) and rotational speed. For flexible and steerable drilling systems, unlike rigid drilling tools, the interaction between operational parameters is further complicated by the flexible nature of the drilling instrument and guide tubes, which are prone to deflections and buckling under external forces if not optimally controlled [24]. The current CT-SDR studies lack a systematic characterization approach to identify the optimal drilling parameters and maximize drilling efficiency and trajectory accuracy. This evaluation, therefore, is so critical as non-optimal parameters can lead to issues such as thermal bone necrosis due to excessive heat generation, potential bone damage from inappropriate forces, accelerated instrument wear and failure.

To establish a foundational understanding of the key drilling parameters required for creating J-shaped trajectories with CT-SDRs, and as our main contribution, this paper presents a systematic study characterizing two operational factors (i.e., the drill feed rate and rotational speed) across two CT-SDRs integrated with a robotic manipulator. To evaluate the effect of rotational speed on drilling efficacy, we developed two CT-SDR designs: (i) a custom-designed *High-Speed Drill (HSD)* powered by a DC motor capable of providing a rotational speed up to 16,000 RPM, and (ii) a *Low-Speed Drill (LSD)* created by modifying a conventional handheld orthopedic drill, using its motor and gear system to provide a maximum speed of 1,000 RPM. These designs enabled a direct comparison of how drilling parameters affect the performance of a CT-SDR (with its compliant structure and flexible instrument) versus a conventional surgical drill characterized by lower speed, higher torque, and rigid instru-

mentation. This analysis highlights both the similarities and key differences in drilling behavior between flexible robotic drills and traditional handheld systems. Using these two platforms, we conducted rigorous experiments to create J-shaped trajectories under varying rotational and insertion speeds in synthetic Sawbones phantoms with densities ranging from 5–25 PCF, thereby simulating a spectrum of bone qualities encountered in spinal procedures. The comparative study examined performance metrics (hole diameter and trajectory curvature) and operational metrics (drilling time and torque at the drill tip, inferred from motor current). Figure 1 illustrates the HSD/LSD and the systematic framework used to identify optimal operational parameters for J-shaped drilling.

II. Steerable Drilling Robots

To rigorously evaluate the operational parameters for J-shaped drilling, two robotic systems were developed based on the CT-SDR architecture. While both systems share several core design features that enable curved drilling, they differ in their rotational power transmission. In this section, we first describe the common elements of both robots, followed by the specific design modifications introduced for the HSD and LSD robots, as shown in Fig. 1. The CT-SDRs consist of the following key components:

1) NiTinol Guide Tube: It is vital that the CT-SDR accurately reproduces the clinician pre-planned curved trajectories for patient safety. To achieve this, a guiding tool capable of generating precise curved trajectories is required. As demonstrated by Sharma et al. [15], Nitinol (NiTi) tubes are well-suited for this role. Their superelastic properties allow them to return to a pre-defined heat-treated shape, while their biocompatibility supports safe use in surgical environments. In this work, as shown in Fig. 2, we heat treated a 3.6 mm outer diameter (OD) Niti tube (Euroflex GmbH, German) with a 3.1 mm inner diameter (ID) and an arc length of approximately 93 mm. The NiTi tube was further constrained within an stainless steel tube (McMaster-Carr) with a 5 mm OD, 4 mm ID, and length of approximately 85 mm.

2) Flexible Drilling Tool: While the NiTi tube is essential for ensuring that the final curved trajectory matches the clinician's planned trajectory, it must be paired with a custom flexible drilling tool to physically drill the trajectory within bone. The flexible drilling tool consists of a 4.7 mm OD drill bit (8175A74, McMaster-Carr) that is laser welded to a 2.2 mm OD torque coil (Asahi Intecc, USA, Inc.) with a 1.3 mm ID. The torque coil plays a vital role in transmitting rotational force from the motor to the drill tip. For additional stability, the torque coil is further laser welded to a stainless steel tube (51755K13, McMaster-Carr) of 1.5 mm OD diameter. This three-part, laser-welded assembly is then secured through the center of the NiTi guide, enabling precise creation of the prescribed curved trajectory. The flexible drilling tool is shown in Fig. 2.

3) Linear Actuation Units: Figure 1 shows the linear actuation system used for curved drilling. This system is responsible for advancing the NiTi tube, which is held concentrically by the drill chucks along the center of the CT-SDR. During insertion, the NiTi tube is initially kept straight by a surrounding stainless steel tube. As the linear actuator pushes the NiTi tube forward, it exits the stainless steel constraint and recovers its heat-treated curved shape, thereby creating the desired curved drilling trajectory. The linear actuation is driven by NEMA 23 stepper motors (B08ZKF9ZD8, Amazon), controlled through Rtelligent motor drivers (B07S897BZZ, Amazon) and an Arduino Nano interface.

4) Rotational Actuation Units: In addition to linear actuation, precise rotational control of the drill bit is essential for drilling through the bone and generating the planned curved trajectories. Although both HSD and LSD systems rely on the same linear actuation, overall architecture, and flexible drilling tool, they differ in the mechanism used to transmit rotational power to the drill bit, as detailed in the following subsections:

Low Speed CT-SDR (LSD): Conventional rigid drilling tools focus on utilizing low speed and high torque to ensure efficient drilling into harder bone [25]. To replicate the clinical standard, a commercially available surgical drill (256919266906,eBay) was disassembled and integrated into the CT-SDR. This conventional drilling system combined with our CT-SDR system enables us to create curvilinear trajectories while ensuring compliance with current drilling methods. The maximum speed of the surgical drill was measured as 1000 RPM using a tachometer (R7050, REED Instruments).

High Speed CT-SDR (HSD): As the CT-SDR is expected to reliably created curvilinear trajectories, it is vital to take into account the additional forces that can affect it compared to conventional drilling tools. For instance, while conventional rigid drilling instruments are only expected to go linearly, the curvilinear trajectory of the CT-SDR can lead to additional frictional forces due to increased contact with the surrounding environment [13], [24], [25]. To account for this additional loads, it is vital that the drill can rotate at a higher speed to prevent any stalling or rotational speed loss during the drilling process. Towards this, a high powered DC motor (B09XM8FDVR, Amazon) is utilized to compensate for any power loss. This high powered DC motor can go at a maximum speed of 16000 RPM.

III. Experimental Evaluation

A. Experimental Set-Up

Figure 2 illustrates the experimental setup for the LSD and HSD characterization studies. The setup includes a 7-DOF robotic arm (KUKA LBR 14 Med, Germany), LSD and HSD CT-SDRs, and Sawbones blocks (Pacific Research Laboratories, USA) of varying densities including PCF 10, 15, 20, and 25 ($0.16, 0.24, 0.32,$ and 0.40 g $\cdot$ cm^{-3}, respectively). Of note, PCFs below 15 simulate bones with low mineral density (i.e., osteoporotic bone), PCF 20 represents low density of heathy cancellous bone, and values above 20 correspond to higher densities of cancellous bone [26]. For this study, we assumed, without loss of generality, that a surgeon selected an 18 mm straight drilling trajectory and a

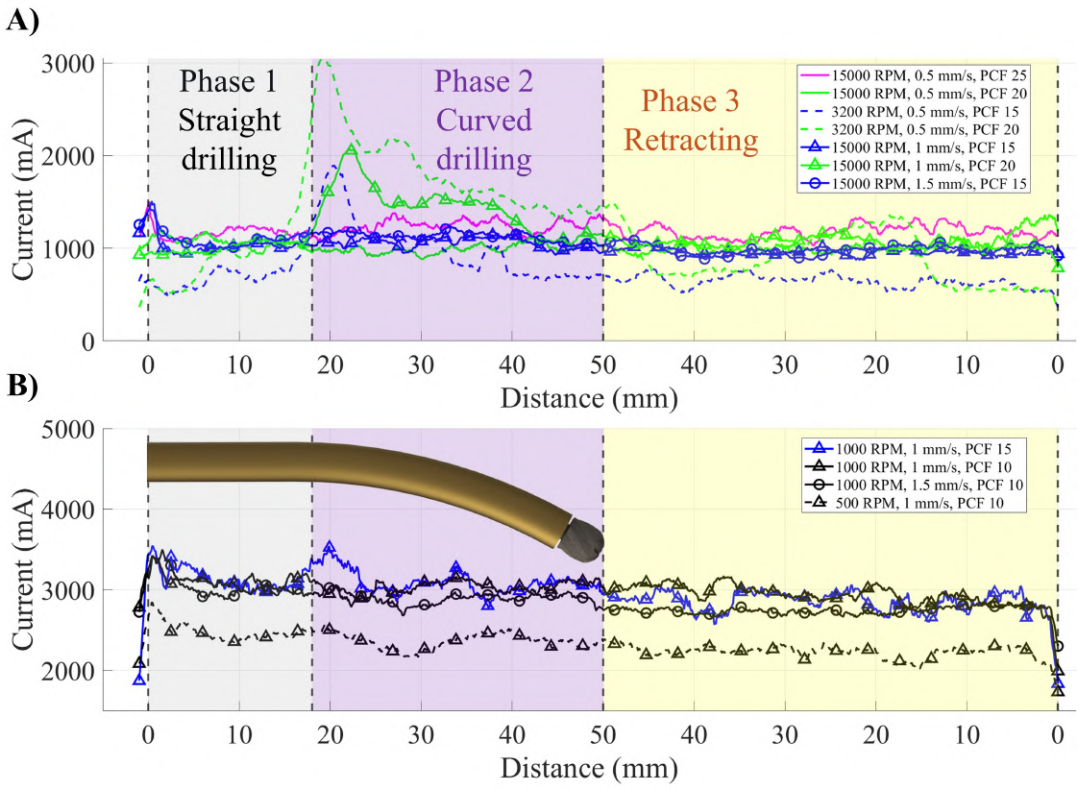

Fig. 3. Measured drilling current profiles for varying feed rates, rotational speeds, and Sawbones PCFs (A) High-speed drill results showing current response across three phases: Phase 1 (straight drilling), Phase 2 (curved drilling), and Phase 3 (retraction). (B) Low-speed drill results for same procedure with CT-SDR overlaid on top to correspond to phases.

32 mm curved trajectory to replicate a realistic SF procedure for an L3 vertebra [27]. The chosen curved trajectory had a radius of curvature of 117 mm.

B. Experimental Procedure

Prior to drilling, sawbones blocks with densities ranging from PCF 10 to PCF 25 were used in this study, as they replicate bone properties from moderately osteoporotic bone to healthy cancellous bone [26]. Each Sawbones sample was secured to a 3D-printed PLA resin fixture (fabricated using a Raise3D printer, Raise3D Technologies Inc.), which was then mounted onto an optical table. After fixation, the Low-Speed Drill (LSD) was attached to the KUKA robotic arm and autonomously aligned with the Sawbones surface. Drilling was initiated by accelerating the drill to a rotational speed of 500 mm/s, after which the robotic arm advanced linearly to drill an 18 mm straight trajectory at a feed rate of 0.5 mm/s. The remaining 32 mm of the planned curved trajectory was executed using a joystick interface.

During drilling, motor current data was collected using an ACS712 current sensor (ACS712ELC30A, HiLetgo) connected to an Arduino Nano microcontroller to quantify the current drawn by the rotational motor. These measurements were used to estimate the torque required for drilling into Sawbones of varying densities. Following completion of each trajectory, the drill was retracted, and different combinations of Sawbones densities and drilling parameters were tested. An identical experimental procedure was also performed using the High-Speed Drill (HSD) system.

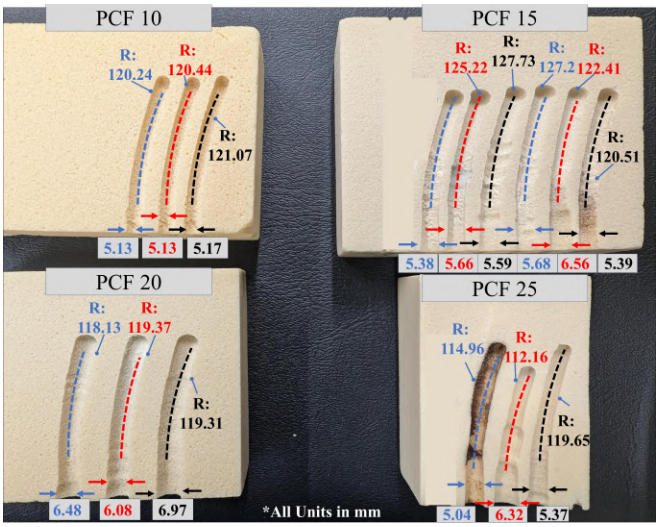

Fig. 4. Representative Sawbones samples after drilling, measured for hole diameter and radius of curvature for PCF 10, 15, 20, and 25. All dimensions are reported in millimeters (mm).

After drilling, the pilot hole diameter was measured using calipers, and the Sawbones blocks were halved for further analysis. The cross-sections of the halved samples were imported into SolidWorks (Dassault Systèmes, France) for quantitative evaluation of the radius of curvature of the drilled trajectories. Representative cross-sections from the HSD system, along with the measured hole diameters and

radii of curvature, are shown in Fig. 4.

C. Experimental Parameters

To fully characterize both drilling systems under different conditions, we tested Sawbones blocks of varying densities across a range of speed parameters. Preliminary studies were first conducted to determine the capability of each CT-SDR, specifically identifying the maximum Sawbones density and the allowable combinations of linear and rotational speeds each drill could achieve. From these initial experiments, we found that the Low-Speed Drill (LSD) was only capable of drilling into PCF 10 and PCF 15 blocks, whereas the High-Speed Drill (HSD) could reliably be evaluated on PCF 15, PCF 20, and PCF 25 blocks. For the LSD, rotational speeds of 500 RPM (minimum) and 1000 RPM (maximum) were paired with translational feed rates ranging from 0.5 to 1.5 mm/s. These limits were selected based on the drill's operating range and prior CT-SDR studies [15], [28]. For the HSD, rotational speeds of 3200 RPM and 15,000 RPM were tested, combined with the same translational feed rate range (0.5–1.5 mm/s). HSD was not tested on PCF 10 blocks, as preliminary trials indicated it could easily drill through this density without difficulty. Table I summarizes the tested parameters. For consistency with Fig. 1, we adopt the notation ${}^{i}_{j}\mathrm{D}^{k}$, where i denotes the rotational speed, j the feed rate, D the drill type (LSD or HSD), and k the PCF density.

IV. Results and Discussion

To fully characterize both high speed and low speed CT-SDR systems, it is vital to characterize their behaviors using multiple metrics for the various drilling parameters tested. These metrics offer insight into both the cutting torque required for drilling across varying bone densities and the efficacy of producing clinician-desired trajectories and pilot holes efficiently.

A. Motor Current

Figure 3-A illustrates the current data collected from the HSD during the drilling process and Fig. 3-B illustrates the current data for the LSD. To ensure the repeatability of the results, each plotted line represents the average of three separate trials. The drilling process consists of three phases: straight drilling for 18 mm, curved drilling for 32 mm, and finally retraction of the drill to exit from the drilled hole. The current over time for the HSD, shown in 3-A, highlights the distinct power requirements of each drilling phase. A minor current spike is observed at the start, corresponding to the initial contact between the drill bit and the Sawbones. During the straight drilling phase (Phase 1), the current stabilizes at a baseline of approximately 1066 mA, indicating a steady cutting process. As the tool transitions from the straight to the curved trajectory (Phase 2), a prominent spike occurs, which can be attributed to the increased torque needed to alter the drill's path. The current then settles at a higher average of approximately 1433 mA, confirming that navigating the curved path requires significantly more torque than straight

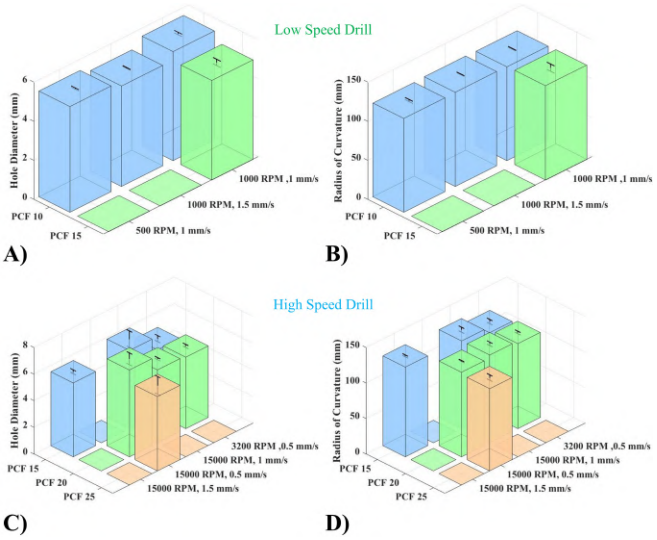

Fig. 5. Comparative 3D analysis of drilling outcomes as a function of feed rate, rotational speed, and phantom density (PCF). A) The hole diameter for LSD, B) radius of curvature for LSD, C) hole diameter, and D) radius of curvature.

drilling. In the final retraction phase (Phase 3), the average current drops below the level of the insertion phases but remains above the no-load current, as the flutes of the drill bit still engage with the bone phantom while being retracted.

Figure 3-B shows the results for the LSD, which displayed a significantly higher baseline current, between 2800 mA and 3500 mA. This elevated current is a direct consequence of the LSD's geared motor, which requires more power to overcome the inherent friction and mechanical disadvantage of the gear train. Of note, once this higher energy threshold is met, the current remains relatively stable throughout the drilling process, even during the transition from straight to curved drilling. This suggests that the internal friction of the geared system is the dominant factor in the motor's current draw, masking the more subtle variations in torque that arise from the drill bit's interaction with the Sawbones. This is further supported by the observation that the lowest speed setting (500 RPM) corresponded to the lowest overall current, as the reduced speed lessens the dynamic friction within the gearbox.

A closer examination of the current profiles reveals distinct trends related to rotational speed and feed rate. Specifically, a sharp increase in current is observed for the 3200 RPM tests, particularly in the denser PCF 15 and PCF 20 phantoms, and also for the 15,000 RPM test at a 1 mm/s feed rate in PCF 20. This indicates that lower rotational speeds require greater torque to cut the material, resulting in a higher current draw. A similar trend is observed when comparing results at the same rotational speed but with different feed rates, where faster insertion speeds lead to an increased current demand. Furthermore, the current signals for cases with lower rotational speeds or higher feed rates exhibit more variability. Conversely, conditions with higher RPM and lower feed rates produce smoother, more stable profiles. This stability can be attributed to a more controlled cutting action; at higher rotational speeds and lower feed rates, the drill

removes material more consistently, reducing fluctuations in torque.

B. Hole Diameter

Table I and Figure 5 report the hole diameters measured from the LSD and HSD, while Figure 4 presents a representative sample of measurements across the different PCF Sawbones specimens. As expected, the LSD was only effective in lower-density phantoms, with drilling success tapering off beyond PCF 15. At 1000 RPM, a slower feed rate produced a larger hole diameter (5.59 mm at 1 mm/s versus 5.14 mm at 1.5 mm/s). This enlargement is likely due to increased drill tip engagement with the medium at lower feed rates, where prolonged tool-material interaction allows for more lateral deviation. With the feed rate held constant, the 500 RPM trials generated a hole diameter similar to the 1000 RPM trials (5.42 mm versus 5.59 mm), suggesting minimal influence of rotational speed in this range. Additionally, lower-density phantoms yielded larger holes (5.59 mm at PCF 10 versus 5.10 mm at PCF 15), which is consistent with softer material permitting greater tool deflection.

Comparable trends were observed in the HSD results. At 15,000 RPM in PCF 15, a lower feed rate again produced a larger hole diameter (5.87 mm at 1 mm/s versus 5.54 mm at 1.5 mm/s), reinforcing the effect of feed rate on drill tip deflection. Hole diameter generally decreased with increasing phantom density. This is because the denser, more rigid material provides better lateral support, constraining the flexible drill and minimizing deflection. Taken together, these findings indicate that slower feed rates, while enabling more controlled drilling, can increase drill tip deflection and enlarge the resulting channel. These results are also in good agreement with those reported in [25].

C. Radius of Curvature

Table I and Figure 5 report the radius of curvature for the drilled trajectories performed using both HSD and LSD with multiple combinations of drilling parameters and Figure 4 presents a representative sample of measurements across the different PCF Sawbones specimens. The radius of curvature (RoC) was also analyzed for both drills. For the LSD, which was only capable of drilling in the lower-density phantoms (PCF 10 and 15), only small differences in RoC were observed across the tested parameters, with all values clustering around 120 mm. This consistency is likely because the softer material offered less resistance and therefore less opportunity for significant trajectory deviation. In contrast, the HSD showed more distinct trends. At a constant rotational speed, higher feed rates produced larger RoCs, resulting in straighter trajectories. For instance, at 15,000 RPM in PCF 20, the 1.5 mm/s feed rate resulted in a higher RoC (126.28 mm) compared to the 1 mm/s feed rate (123.37 mm). Similarly, at 3200 RPM in PCF 20, the RoC increased from 119.56 mm at 0.5 mm/s to 123.47 mm at 1 mm/s. This trend suggests that a faster insertion rate increases the deformation of the guide tube, which in turn reduces the achievable curvature, a finding consistent with observations reported by Sharma et al. [15]. No specific pattern was observed when comparing tests at similar feed rates but different rotational speeds. However, when comparing drilling in different densities at 15,000 RPM and 0.5 mm/s, the denser Sawbones (PCF 25) produced a tighter RoC (115.59 mm) compared to PCF 20 (118.94 mm). This indicates that higher density materials exert greater reaction forces on the guide tube, leading to a more pronounced curvature. At higher feed rates (1 mm/s), the RoCs were similar across the different densities.

D. Drilling Time

Based on the data in Table I, drilling time is primarily determined by the feed rate. As expected, faster feed rates completed the trajectory more quickly, with the 1.5 mm/s insertions averaging approximately 36 seconds. At 1 mm/s, the average time increased to roughly 50 seconds, while the slowest feed rate of 0.5 mm/s required more than 100 seconds on average for each parameter combination. This direct relationship between feed rate and drilling time highlights a critical trade-off in a clinical setting. The selection of an appropriate feed rate would depend on procedural requirements, balancing the need for surgical efficiency with the demands of the specific anatomy. For instance, a surgeon might select a slower, more deliberate feed rate when working with low-density or osteoporotic bone to reduce overall operative time. Conversely, a slower feed rate might be chosen in denser bone to provide the desired trajectory accuracy and hole quality.

E. Comprehensive Analysis for Clinical Application

The characterization of these drilling parameters provides a clear guideline for optimizing surgical technique in real-time clinical scenarios. The choice of drilling parameters is not straightforward and involves a series of trade-offs between speed, accuracy, and the quality of the resulting pilot hole. Based on our findings, we can outline a set of recommendations for surgeons using steerable drilling systems. For procedures in patients with low bone density or osteoporosis (simulated by PCF 10 and 15), a low rotational speed can be sufficient. However, for denser bone (PCF 20 and above), a high rotation speed is essential to ensure the successful completion of the trajectory. The higher rotational speed and more stable cutting action of the HSD are necessary to overcome the increased material resistance.

The selection of feed rate presents a critical trade-off between surgical efficiency and accuracy. While a faster feed rate significantly reduces drilling time, it also leads to a larger radius of curvature (a straighter path) and a larger hole diameter. The straighter path may be clinically undesirable when a specific curved trajectory is needed to avoid critical anatomy. Furthermore, the resulting oversized hole could compromise the pull-out strength of a pedicle screw. Therefore, a surgeon should select the feed rate based on the specific anatomical constraints of the procedure. A slower feed rate is recommended when a tight curvature is required or when drilling in close proximity to sensitive

TABLE I

EXPERIMENTAL RESULTS FOR DIFFERENT PARAMETER CONFIGURATIONS.

Configuration	**Hole Diameter** (mm)	**Radius of Curvature** (mm)	**Total Time** (s)
${}^{15000}\text{HSD}^{25}_{0.5}$	5.57 ± 0.66	115.59 ± 3.78	106.67 ± 0.58
${}^{15000}\text{HSD}^{20}_{0.5}$	6.51 ± 0.44	118.94 ± 0.70	107.33 ± 2.08
${}^{3200}\text{HSD}^{15}_{0.5}$	4.86 ± 0.23	115.09 ± 3.00	104.67 ± 1.53
${}^{3200}\text{HSD}^{20}_{0.5}$	5.36 ± 0.11	119.56 ± 1.69	107.67 ± 3.06
${}^{15000}\text{HSD}^{20}_{1.0}$	5.46 ± 0.08	123.47 ± 2.38	55.00 ± 1.73
${}^{15000}\text{HSD}^{15}_{1.0}$	5.87 ± 0.61	123.37 ± 3.44	51.33 ± 0.58
${}^{15000}\text{HSD}^{15}_{1.5}$	5.54 ± 0.14	126.28 ± 1.30	37.00 ± 1.00
${}^{1000}\text{LSD}^{15}_{1.0}$	5.10 ± 0.16	120.04 ± 4.66	54.67 ± 0.58
${}^{1000}\text{LSD}^{10}_{1.0}$	5.59 ± 0.07	120.11 ± 0.05	53.33 ± 0.58
${}^{1000}\text{LSD}^{10}_{1.5}$	5.14 ± 0.02	120.58 ± 0.43	35.33 ± 1.15
${}^{500}\text{LSD}^{10}_{1.0}$	5.42 ± 0.03	119.95 ± 1.35	53.33 ± 0.58

structures, as it provides greater control and a more accurate trajectory.

Finally, the combination of high rotational speed and a low feed rate appears to offer the most stable and controlled drilling performance, as evidenced by the smoother current profiles. This combination minimizes torque fluctuations and provides a more consistent cutting action, which is ideal for critical and precision applications. By understanding these relationships, a surgeon can intelligently select the optimal drilling parameters to balance the competing demands of speed, accuracy, and patient safety.

V. CONCLUSION

This paper presents a comprehensive characterization of two Concentric Tube Steerable Drilling Robots (CT-SDRs): a low-speed and a high-speed system. This study therefore can serve as a guide for design choices, component selection, and operational control tailored to patient-specific bone quality. Our analysis of rotational speed, feed rate, and bone phantom density highlights critical performance trade-offs. We show that high-speed drilling is essential for penetrating dense bone, while slower feed rates, though more time-consuming, enhance trajectory accuracy and minimize hole enlargement. These findings provide quantitative guidelines for surgeons to select optimal drilling parameters based on anatomy and procedural goals, effectively balancing surgical efficiency with precision. Future work will extend this evaluation to animal and cadaveric specimens to verify the accuracy of the obtained results under more clinically realistic conditions. In addition, the steerable drilling robot will be integrated with OFDR-based shape sensing as a feedback of the drilling trajectories [29], [30]. Furthermore, we will extend this system to other complex anatomical trajectories (i.e., pelvis) and include osteotomy to enable a holistic joint osteotomy and implant fixation system [31]–[33].

REFERENCES

[1] R. W. Gaines Jr, "The use of pedicle-screw internal fixation for the operative treatment of spinal disorders," *JBJS*, vol. 82, no. 10, p. 1458, 2000.

[2] E. Rometsch, M. Spruit, J. E. Zigler, V. K. Menon, J. A. Ouellet, C. Mazel, R. Härtl, K. Espinoza, and F. Kandziora, "Screw-related complications after instrumentation of the osteoporotic spine: a systematic literature review with meta-analysis," *Global spine journal*, vol. 10, no. 1, pp. 69–88, 2020.

[3] L. Weiser, G. Huber, K. Sellenschloh, L. Viezens, K. Püschel, M. M. Morlock, and W. Lehmann, "Insufficient stability of pedicle screws in osteoporotic vertebrae: biomechanical correlation of bone mineral density and pedicle screw fixation strength," *European Spine Journal*, vol. 26, no. 11, pp. 2891–2897, 2017.

[4] R. Wittenberg, M. Shea, D. Swartz, K. Lee, A. White 3rd, and W. Hayes, "Importance of bone mineral density in instrumented spine fusions." *Spine*, vol. 16, no. 6, pp. 647–652, 1991.

[5] H. Ding, B. Han, Y. Hai, Y. Liu, L. Guan, A. Pan, and T. Liu, "The feasibility of assessing the cortical bone trajectory screw placement accuracy using a traditional pedicle screw insertion evaluation system," *Clinical spine surgery*, vol. 34, no. 2, pp. E112–E120, 2021.

[6] T. Li, A. Badre, F. Alambeigi, and M. Tavakoli, "Robotic systems and navigation techniques in orthopedics: A historical review," *Applied Sciences*, 2023.

[7] A. Elmi-Terander, G. Burström, R. Nachabe, H. Skúlason, K. Pedersen, M. Fagerlund, F. Ståhl, A. Charalampidis, M. Söderman, S. Holmin, D. Babic, I. Jenniskens, E. Edström, and P. Gerdhem, "Pedicle screw placement using augmented reality surgical navigation with intraoperative 3d imaging," *Spine*, vol. 44, pp. 517 – 525, 2018.

[8] C. L. Goldstein, D. S. Brodke, and T. J. Choma, "Surgical management of spinal conditions in the elderly osteoporotic spine," *Neurosurgery*, vol. 77, pp. S98–S107, 2015.

[9] F. Alambeigi, M. Bakhtiarinejad, A. Azizi, R. Hegeman, I. Iordachita, H. Khanuja, and M. Armand, "Inroads toward robot-assisted internal fixation of bone fractures using a bendable medical screw and the curved drilling technique," in *2018 7th IEEE International Conference on Biomedical Robotics and Biomechatronics (Biorob)*, 2018, pp. 595–600.

[10] F. Alambeigi and M. Armand, "Steerable drill for minimally-invasive surgery," Jan. 2 2020, uS Patent App. 16/490,751.

[11] Y. Wang, H.-W. Yip, H. Zheng, H. Lin, R. Taylor, and K. W. S. Au, "Design and experimental validation of a miniaturized robotic tendon-driven articulated surgical drill for enhancing distal dexterity in minimally invasive spine fusion," *IEEE/ASME Transactions on Mechatronics*, 2021.

[12] F. Alambeigi, M. Bakhtiarinejad, S. Sefati, R. Hegeman, I. Iordachita, H. Khanuja, and M. Armand, "On the use of a continuum manipulator and a bendable medical screw for minimally invasive interventions in orthopedic surgery," *IEEE transactions on medical robotics and bionics*, vol. 1, no. 1, pp. 14–21, 2019.

[13] F. Alambeigi, Y. Wang, S. Sefati, C. Gao, R. J. Murphy, I. Iordachita, R. H. Taylor, H. Khanuja, and M. Armand, "A curved-drilling approach in core decompression of the femoral head osteonecrosis using a continuum manipulator," *IEEE Robotics and Automation Letters*, vol. 2, no. 3, pp. 1480–1487, 2017.

[14] S. Sharma, S. Go, Z. Yakay, Y. Kulkarni, S. Kapuria, J. P. Amadio, R. Rajebi, M. Khadem, N. Navab, and F. Alambeigi, "A patient-specific framework for autonomous spinal fixation via a steerable drilling robot," in *International Conference on Medical Image Computing and Computer-Assisted Intervention*. Springer, 2024, pp. 35–45.

[15] S. Sharma, T. G. Mohanraj, J. P. Amadio, M. Khadem, and F. Alambeigi, "A concentric tube steerable drilling robot for minimally invasive spinal fixation of osteoporotic vertebrae," *IEEE Transactions on Biomedical Engineering*, vol. 70, no. 11, pp. 3017–3027, 2023.

[16] S. Sharma, Y. Sun, J. Bonyun, M. Khadem, J. Amadio, A. H. Eskandari, and F. Alambeigi, "A biomechanics-aware robot-assisted steerable drilling framework for minimally invasive spinal fixation procedures," *IEEE Transactions on Biomedical Engineering*, vol. 71, no. 6, pp. 1810–1819, 2024.

[17] Y. Kulkarni, S. Sharma, S. Go, J. P. Amadio, M. Khadem, and F. Alambeigi, "Towards design and development of a concentric tube steerable drilling robot for creating s-shape tunnels for pelvic fixation procedures," *2025 IEEE/RSJ International Conference on Intelligent Robots and Systems (IROS)*, pp. 19 067–19 072, 2025.

[18] Y. Kulkarni, S. Sharma, Z. Yakay, S. Go, J. P. Amadio, M. Tilton, and F. Alambeigi, "A synergistic patient-specific approach for enhanced spinal fixation using a novel flexible pedicle screw and a complementary steerable drilling robotic system," *IEEE Transactions on Biomedical Engineering*, pp. 1–11, 2025.

[19] Y. Kulkarni, S. Sharma, J. Allison, J. P. Amadio, M. Tilton, and F. Alambeigi, "Towards the feasibility analysis and additive manufacturing of a novel flexible pedicle screw for spinal fixation procedures," *The 35th Annual International Solid Freeform Fabrication Symposium*, pp. 1–11, 2024.

[20] Y. Kulkarni, S. Sharma, O. Rezayof, S. Kapuria, J. P. Amadio, M. Khadem, M. Tilton, and F. Alambeigi, "Augmented bridge spinal fixation: A new concept for addressing pedicle screw pullout via a steerable drilling robot and flexible pedicle screws," in *2025 IEEE/RSJ International Conference on Intelligent Robots and Systems (IROS)*, 2025, pp. 401–406.

[21] D. Maroufi, X. Huang, Y. Kulkarni, O. Rezayof, S. Sharma, V. Goggela, J. P. Amadio, M. Khadem, and F. Alambeigi, "S3d: A spatial steerable surgical drilling framework for robotic spinal fixation procedures," in *2025 IEEE/RSJ International Conference on Intelligent Robots and Systems (IROS)*, 2025, pp. 2156–2162.

[22] S. Sharma, Y. Sun, S. Go, J. P. Amadio, M. Khadem, A. H. Eskandari, and F. Alambeigi, "Towards biomechanics-aware design of a steerable drilling robot for spinal fixation procedures with flexible pedicle screws," in *2023 International Symposium on Medical Robotics (ISMR)*, 2023, pp. 1–6.

[23] S. Sharma, Y. Kulkarni, S. Go, J. Bonyun, J. P. Amadio, M. Tilton, M. Khadem, and F. Alambeigi, "Spatial spinal fixation: A transformative approach using a unique robot-assisted steerable drilling system and flexible pedicle screw," in *2024 IEEE/RSJ International Conference on Intelligent Robots and Systems (IROS)*. IEEE, 2024, pp. 11 018–11 023.

[24] F. Alambeigi, S. Sefati, R. J. Murphy, I. Iordachita, and M. Armand, "Design and characterization of a debriding tool in robot-assisted treatment of osteolysis," in *2016 IEEE International Conference on Robotics and Automation (ICRA)*, 2016, pp. 5664–5669.

[25] F. Alambeigi, Y. Wang, R. J. Murphy, I. Iordachita, and M. Armand, "Toward robot-assisted hard osteolytic lesion treatment using a continuum manipulator," in *2016 38th Annual International Conference of the IEEE Engineering in Medicine and Biology Society (EMBC)*. IEEE, 2016, pp. 5103–5106.

[26] A. Çetin and D. A. Bircan, "Experimental investigation of pull-out performance of pedicle screws at different polyurethane (pu) foam densities," *Proceedings of the Institution of Mechanical Engineers, Part H: Journal of Engineering in Medicine*, vol. 235, no. 6, pp. 709–716, 2021.

[27] M. R. Zindrick, L. L. Wiltse, E. H. Widell, J. C. Thomas, H. Wr, F. Bt, and C. W. Spencer, "A biomechanical study of intrapeduncular screw fixation in the lumbosacral spine." *Clinical orthopaedics and related research*, vol. 203, pp. 99–112, 1986.

[28] S. Sharma, Y. Sun, J. Bonyun, M. Khadem, J. Amadio, A. H. Eskandari, and F. Alambeigi, "A biomechanics-aware robot-assisted steerable drilling framework for minimally invasive spinal fixation procedures," *IEEE Transactions on Biomedical Engineering*, vol. 71, no. 6, pp. 1810–1819, 2024.

[29] M. Tavangarifard, W. R. Ovalle, and F. Alambeigi, "Single-fiber optical frequency domain reflectometry shape sensing of continuum manipulators with planar bending," *ArXiv*, vol. abs/2405.17636, 2024.

[30] Y. Kulkarni, M. Tavangarifard, J. P. Amadio, and F. Alambeigi, "Design and integration of an optical frequency domain reflectometry (ofdr) sensor with a flexible pedicle screw for biomechanical evaluation," in *2025 IEEE/RSJ International Conference on Intelligent Robots and Systems (IROS)*. IEEE, 2025, pp. 2134–2139.

[31] D. Maroufi, Y. Kulkarni, J. E. Bird, J. H. Siewerdsen, and F. Alambeigi, "Comparative analysis of autonomous robotic and manual techniques for ultrasonic sacral osteotomy: A preliminary study," *arXiv preprint arXiv:2602.04076*, 2026.

[32] D. Maroufi, Y. Kulkarni, O. Rezayof, M. Tavangarifard, M. Tilton, J. E. Bird, J. H. Siewerdsen, and F. Alambeigi, "Towards characterization of semi-autonomous robotic partial sacrectomy using an ultrasonic osteotome," in *Medical Imaging 2026: Image-Guided Procedures, Robotic Interventions, and Modeling*. SPIE, 2026, Accepted.

[33] Y. Kulkarni, D. Maroufi, M. Tilton, J. Bird, J. Siewerdsen, and F. Alambeigi, "Towards curved sacroiliac joint fixation using a steerable drilling robot and flexible sacroiliac screws," in *Medical Imaging 2026: Image-Guided Procedures, Robotic Interventions, and Modeling*. SPIE, 2026, Accepted.